LCLS-II Technical Note

LCLS-II TN Hard X-ray Self-Seeding – Impact of Crystal Imperfection on the Wake Fields

LCLS-II TN-17-xx

8/12/17

Yiping Feng

1 Overview

The hard X-ray seeding baseline deliverable for LCLS-II project will be to re-purpose the existing thin diamond crystal based wake-field solution that was implemented for LCLS-I (Amann *et al*., 2012) shown in Figure 1, with the necessary modification to accommodate the change of the X-ray polarization to the vertical direction. It will *not* be used for the LCLS-II high repetition rate hard X-ray FEL beam from 1 to 5 keV, but rather for the low repetition rate (up to 120 Hz) beam generated by the existing normal-conducting Cu Linac and a new variable gap undulator, operating in the photon energy range of 4 to 12 keV, with possible extensions to lower energies to 3 keV and higher energies to 25 keV. The repurposed and modified seeding system is expected to provide comparable seeding performance to the existing LCLS-I system, which worked with an FEL beam generated from a fixed gap undulator and polarized in the horizontal direction. There is *no* seeding deliverable in the photon energy range of 1 to 3 keV, for it requires significant R&D effort in X-ray optics*.

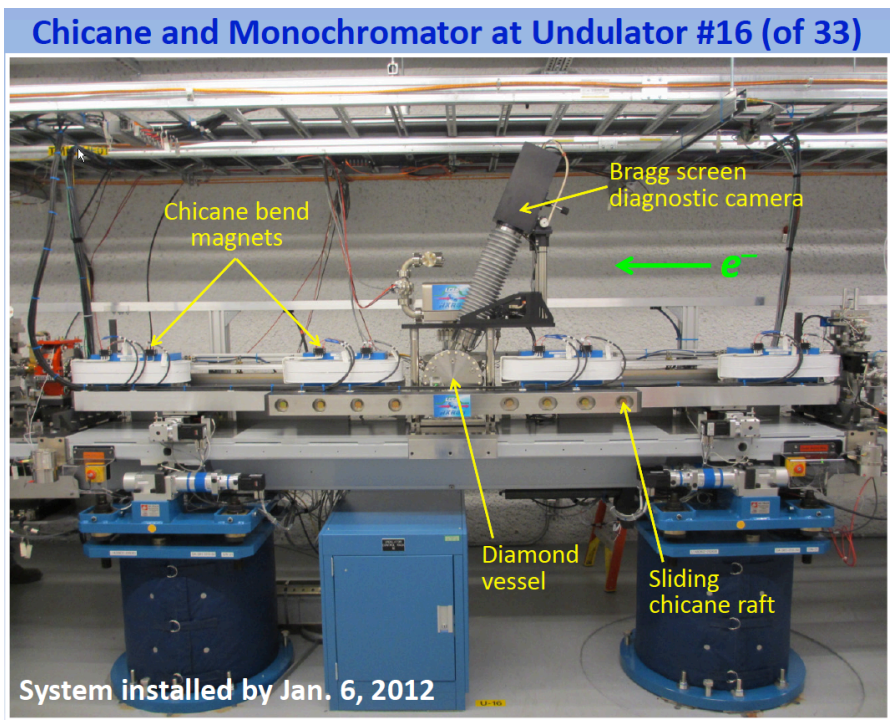

Figure 1. The hard X-ray self-seeding system installed in the LCLS-I undulator hall in unit #16, upstream of undulator #17 and downstream of undulator #15. The main components are the vacuum vessel hosting the thin diamond crystal and the magnetic chicane for temporal and spatial overlap.

1.1 Hard X-ray self-seeding based on Bragg forward scattering

The LCLS-I hard X-ray seeding solution was is based on the self-seeding principle shown in Figure 2, whereby an X-ray seed γ_s is generated from a broadband SASE beam γ produced in the

* Although conceivably a reflection grating based solution could be used from 1 keV and up to possibly 2 keV, and a silicon crystal working in Bragg reflection geometry could cover the 2 to 3 keV energy range, albeit challenging issues remain in high absorption loss and a scattering geometry close to that of back-scattering, creating long optical delay that might require using the fresh bunch technique.

upstream undulator section and diffracting off a thin crystal. The quasi-monochromatic seed(s) is contained in the forward Bragg scattered beam in transmission and delayed in time by many femtoseconds from the main SASE peak. A magnetic chicane is then used to delay the same electron bunch e^- to re-overlap temporally and spatially with the seed γ_s in the downstream undulator section for amplification, in addition to washing out the effect of the micro-bunching already developed in the upstream undulator (Geloni, Kocharyan, and Saldin 2010a; Geloni, Kocharyan, and Saldin 2010b). This scheme was successfully demonstrated (Amann *et al.*, 2012) and has been part of the LCLS-I enhanced FEL production capabilities for the users.

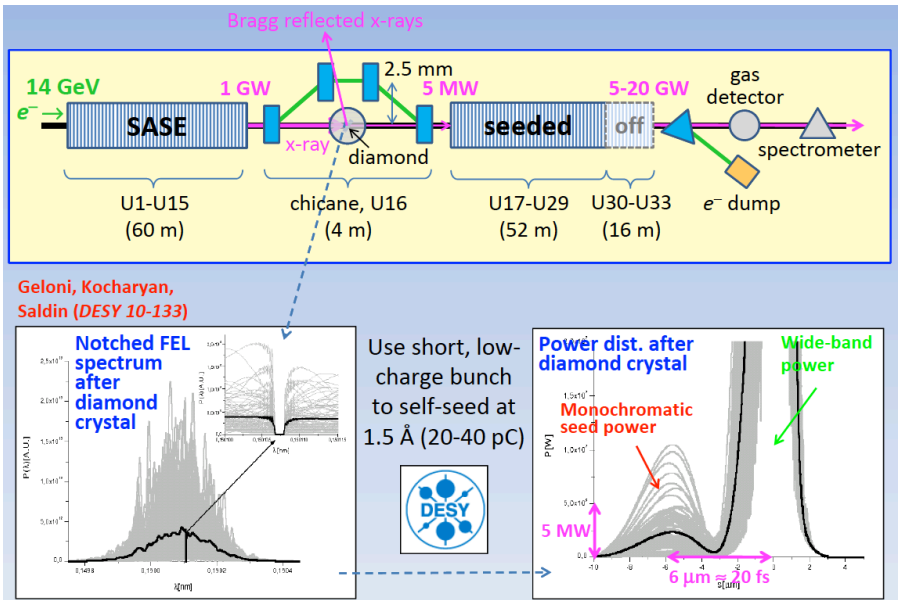

Figure 2. Operating principle of the hard X-ray self-seeding implemented for LCLS-I. The quasi-monochromatic seed emerges from the forward Bragg scattered beam with a time delay of many femtoseconds[†].

1.1.1 Existing crystal arrangement for LCLS-I horizontal polarization

The LCLS-I undulator produces linearly polarized X-ray FEL radiation in the horizontal direction as shown in Figure 3. The thin crystal was oriented in such a way that the diffraction plane ends up normal to the polarization $\boldsymbol{p}$, i.e., being in the σ-geometry. The SASE beam γ was designed to impinge at the center of the crystal and define the beam axis $\boldsymbol{z}$, while the rotation axis $\boldsymbol{x}$ of the pitch (incidence) angle[‡] θ was designed to also cross at the center of the crystal and to be perpendicular to $\boldsymbol{z}$. The beam axis of the electron bunch e^- was shifted from the beam axis $\boldsymbol{x}$ by an amount δh as required by the minimum stay-clear. When tuning the seeding energy by rotating the crystal about the $\boldsymbol{x}$ axis, the beam clearance δh remained unchanged, and there was little walking of the beam on the crystal within the tolerances of mechanical assembly. The decision to use the σ-geometry for diffraction was based on the fact that the scattering would yield the

[†] The Bragg reflected beam is also perfectly good for seeding, but cannot be easily utilized due to diffraction geometry unless additional crystals are used to bring it back into the electron beam path. Even then, the optical delay is so long that again a fresh-bunch technique is needed.

[‡] The Bragg angle $\theta_B = \theta$ if scatter symmetrically; whereas $\theta_B = \theta \pm \alpha$, if scatter asymmetrically, where α is the angle between the crystal surface and the Bragg planes.

maximum seed power regardless of the scattering angle $2\theta_B$, i.e., the polarization factor $\cos^2(2\boldsymbol{p}\hat{}\boldsymbol{o})$ is always equal to unity, where $\boldsymbol{o}$ is the polarization of the scattered radiation.

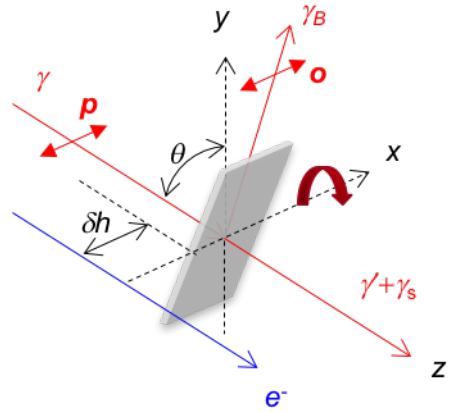

Figure 3. Schematics of the existing hard X-ray self-seeding arrangement for LCLS-I. The beam axis $\boldsymbol{z}$ and rotation axis $\boldsymbol{x}$ are orthogonal and in the horizontal plane. The electron beam axis is also in the horizontal plane but offsets from $\boldsymbol{x}$ by an amount δh from the edge of the crystal. The FEL polarization $\boldsymbol{p}$ is in the horizontal plane as well, normal to the diffraction plane in the vertical, resulting in the σ diffraction geometry.

1.1.2 New crystal arrangement for LCLS-II vertical polarization

A change was made for the LCLS-II variable gap undulator to produce linearly polarized X-ray FEL radiation in the vertical direction as shown in Figure 4. To accommodate this polarization rotation, studies were done to assess the impact on the seeding performance if the existing LCLS-I hard X-ray self-seeding system shown in Figure 1 were to be simply repurposed without any material modifications, including the relative location in the undulator system. It was found that the seed power would have been reduced by the polarization factor $\cos^2(2\boldsymbol{p}\hat{}\boldsymbol{o}) = \cos^2(2\theta_B)$, and since the energy coverage of the installed diamond crystal was such that the Bragg angles were not too far from 45°, the reduction in the seed power would have been quite substantial. The simplest option considered was to rotate the entire existing seeding system by 90°, making the change in polarization complete transparent to the downstream undulators. This option, however, would have resulted in major mechanical interference issues and was deemed not viable. The final decision was then made to make certain modifications to the crystal itself and its rotation assembly, but not the magnetic chicane.

In the new arrangement, the diamond thin crystal will be oriented with its surface normal in the horizontal plane, and the diffraction plane will also be in the horizontal plane and normal to the polarization $\boldsymbol{p}$, thus retaining the σ-geometry. The SASE beam γ, which defines the beam axis $\boldsymbol{z}$, will impinge in the center part of the crystal, and the rotation axis of the pitch angle θ is now in the vertical direction $\boldsymbol{y}$ and still perpendicular to $\boldsymbol{z}$, but does not cross at the center of the crystal. Instead, axis $\boldsymbol{y}$ will be pivoted close to the edge of the crystal such that the clearance between the crystal δh and the electron beam will not be greatly affected while varying the incidence angle. The axis of the electron bunch e^- will be kept at a similar distance from the $\boldsymbol{z}$ axis. The off-axis pivoting on the crystal edge would result in certain degree of beam walking on the crystal, an undesirable consequence of the compromises made to not modify the magnetic chicane, and immediately raises the question as to whether or not the peripheral area of the crystal is just as good as the center that seeding performance is not at all impacted. This is because that the

original crystal that was ultimately chosen to be installed in the LCLS-I system was more perfect and had less defects at the center based on X-ray topographical measurement. However, a quick check by moving the crystal close to the edge did not reveal discernable degradation to the seeding quality.

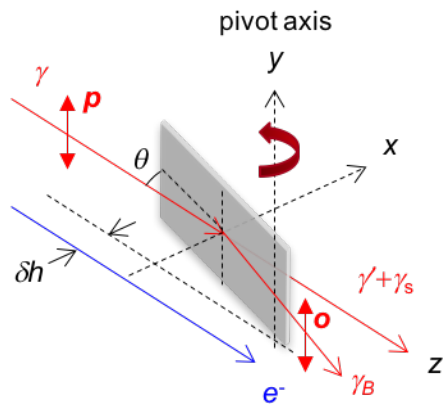

Figure 4. Schematics of the new hard X-ray self-seeding arrangement for LCLS-II. The beam axis ***z*** and rotation axis ***x*** are orthogonal and in the vertical plane. The electron beam axis remains in the horizontal plane but offsets from ***x*** by an amount δh from the edge of the crystal. The FEL polarization ***p*** is in the vertical plane, normal to the diffraction plane in the horizontal, retaining the σ diffraction geometry.

The installed crystal is a 100 μm thick diamond with a [001] cut. The possible extension of the operating energy range to below 4 keV would require either a thinner, i.e., ~ 58 μm, crystal of the [001] cut, or a [111] cut of similar thickness at 100 μm. This is due to the consideration that transmission through the thin crystal becomes more important when going to lower photon energies. If the installed [001] cut crystal is used to diffract asymmetrically off the [111] planes to go below 4 keV to 3 keV, the crystal will be at an oblique angle of 35.26°, effectively increasing the crystal thickness by 73% to 173 μm and reducing the seed power by a factor of 10 to only 0.4% transmission. This is the recommendation by the review committees to include a dual crystal option as an additional modification to the existing system.

The dual diamond crystal option of a) a thinner 58 μm [001] cut crystal or b) a similar thickness of 100 μm [111] cut crystal could introduce potential issues with the lattice quality. A thinner sample is more prone to mechanical strain from mounting, since the mechanical rigidity is proportional to the third power of the thickness. A [111] cut crystal is more difficult to polish, and is more prone to surface roughness and nonuniformity, thus resulting in wavefront distortions related to phase errors. This note will be focusing on the impact of either bending or phase errors on the seeding performance by using X-ray dynamic diffraction calculations to examine the extent of the distortions in the seed fields induced by the crystal imperfections.

2 Seeding wakefield calculations

Hard X-ray self-seeding based on Bragg forward scattering was first proposed by Geloni, Kocharyan, and Saldin, and a *numerical* treatment of the seed field was provided specially for a perfect thin diamond crystal using the Kramers-Kronig relations (Geloni, Kocharyan, and Saldin 2010a; Geloni, Kocharyan, and Saldin 2010b). The amplitude and relative delay of the quasi-monochromatic "seed" or "wakefield" in transmission were computed for a large number of single shots of the SASE field from the upstream undulators. Later Lindberg and Shvyd'ko put forth a different treatment within the general framework of the X-ray dynamical theory but calculating only the Forward Bragg Diffraction (FBD) component for a ultrashort and laterally finite X-ray pulse. They were able to obtain *analytical* expressions for the spatiotemporal distribution and power of the wakefield, which included other interesting effects such as the dependence on the crystal thickness and a transverse spatial shift linked to the temporal delay (Lindberg and Shvyd'ko, 2012; Shvyd'ko and Lindberg, 2012). To calculate the impact of lattice imperfections on the wakefield, we will stay with the approach laid out in the original proposal of the technique (Geloni, Kocharyan, and Saldin 2010a; Geloni, Kocharyan, and Saldin 2010b), but also only account for the FBD part of transmitted beam. First, we show the results on perfect crystals using an input field of a) a Green's function at a small time offset with a perfect wavefront, and b) simulated SASE field generated from Start-To-End (S2E) simulations with a perfect wavefront, for three different photon energies at 4, 8 and 12 keV (Marcus, 2017). The results on strained crystals are then presented for both kinds of input by re-formulating the calculation to that of a perfect crystal but a distorted wavefront. No proof of the validity of the re-formulation will be given, and the findings should be taken as a more practical and convenient approximation to a more rigorous and difficult treatment, one that possibly involves methods like the multi-lamellar approximation for bent crystals or the Penning-Polder approximation for bent Laue crystals, or solving the Takagi-Taupin equations for X-ray dynamical scattering from strained crystals (Takagi and Wills 1962; Taupin, 1964).

2.1 Wakefields for perfect crystals

In the approach taken by Geloni, Kocharyan, and Saldin (Geloni, Kocharyan, and Saldin 2010a; Geloni, Kocharyan, and Saldin 2010b), the spectral property of a thin perfect crystal at the Bragg condition could be obtained by using the scientific computational software XOP2.4 (*https://www1.aps.anl.gov/Science/Scientific-Software/XOP*) toolkit for perfect crystals, where both the reflectivity $R(\omega)$ or transmissivity $T(\omega)$ can be calculated and given in either the σ- or π-geometry for a linearly polarized beam at a given frequency ω. The amplitude of the field $\varepsilon_T(\omega)$ in transmission at ω is simply taken as square-root of the intensity, i.e., $\varepsilon_T(\omega) = \sqrt{\{T(\omega)\}}$. The phase of the frequency component $\phi_T(\omega)$, is related to the amplitude via the Kramers-Kronig relations, and thus can be computed accordingly. The pair $\{\varepsilon_T(\omega), \phi_T(\omega)\}$ allows the calculation of any input field via Fourier transform and then its inverse transform.

The wavefront is assumed to be perfectly flat upon incidence onto the crystal, i.e., the incident angle θ is exactly given by the beam propagation direction z and the crystal surface for symmetric reflections as shown in Figure 5. For asymmetric reflections, the incidence angle is modified by the asymmetric angle Θ. Given the geometry of how the diamond crystal was mounted in the seeding vessel, the reflections used to cover the energy range were the symmetric [004] at 12 keV, symmetric [004] at 8 keV, and asymmetric [111] at 4 keV using the [001] cut with an

asymmetric angle Θ of 54.7356° from the surface. The scattering is always in the σ geometry as shown in Figure 4. The thickness of the diamond is assumed to be 100 μm.

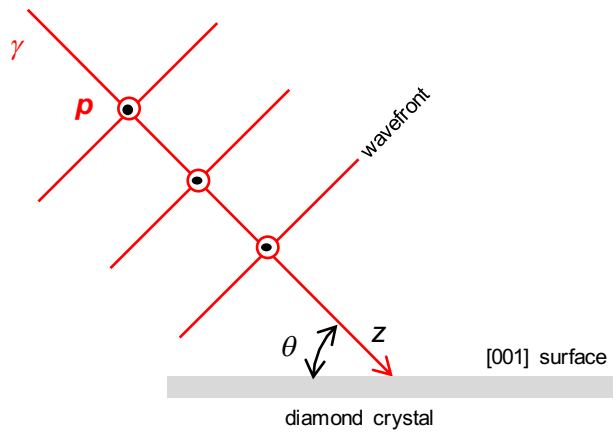

Figure 5. Incident FEL beam with a perfect wavefront onto the diamond crystal. The incident angle is simply given by the angle θ between the beam propagation direction z and the surface of the crystal for symmetric reflections. For asymmetric reflections, the incidence angle must be modified by the asymmetric angle Θ. $\boldsymbol{p}$ is a unit vectors, indicating the polarization in the σ scattering geometry.

2.1.1 Input field of a Green's function in time with a perfect wavefront

First, we show the results for an input field of a quasi- delta-function in time at t_0 = 2.536 fs, which was assumed to have the a Gaussian lineshape with an arbitrary maximum and a FWHM in intensity of 0.082 fs, and a flat phase across the pulse duration. The intensity of the wakefield is shown in Figure 6, Figure 7 and Figure 8, for photon energies of 12, 8 and 4 keV, respectively.

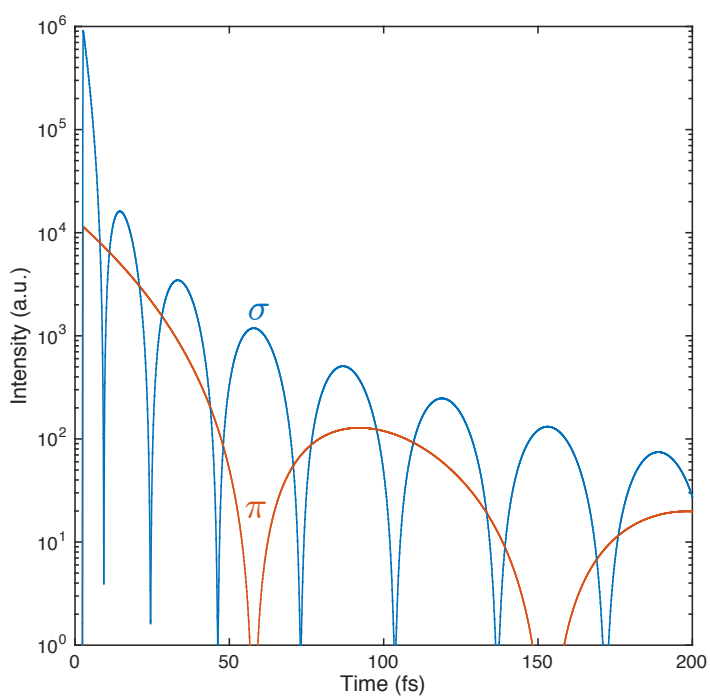

Figure 6. The wakefield intensity including only the Forward Bragg Diffraction (FBD) part of the total transmitted beam at 12 keV of the diamond [004] symmetric reflection. The light blue curve is for the σ scattering geometry, and the brown curve for the π geometry for comparison.

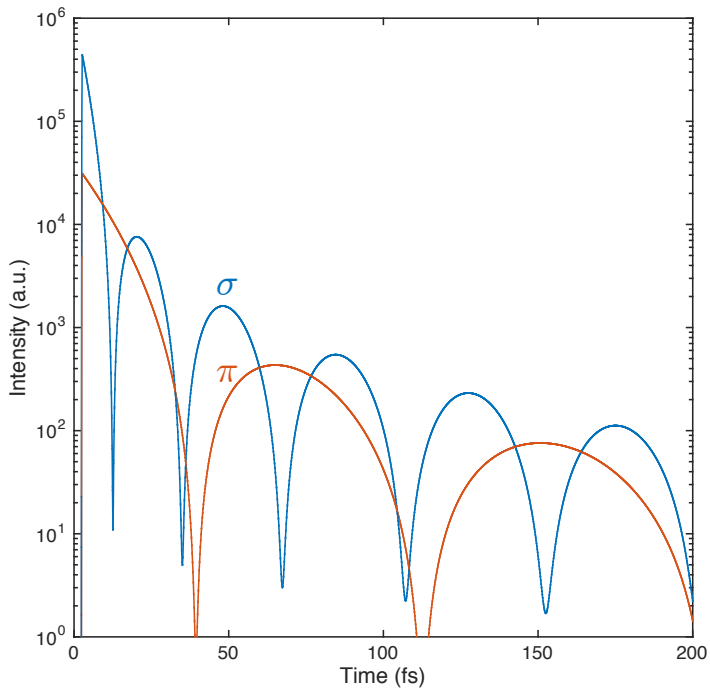

Figure 7. The wakefield intensity including only the Forward Bragg Diffraction (FBD) part of the total transmitted beam at 8 keV of the diamond [004] symmetric reflection. The light blue curve is for the σ scattering geometry, and the brown curve for the π geometry for comparison.

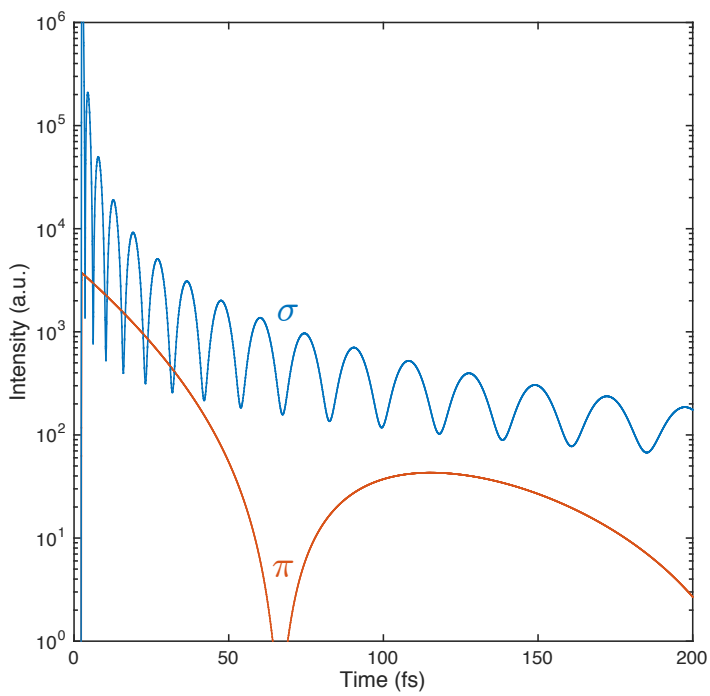

Figure 8. The wakefield intensity including only the Forward Bragg Diffraction (FBD) part of the total transmitted beam at 4 keV of the diamond [111] asymmetric reflection. The light blue curve is for the σ scattering geometry, and the brown curve for the π geometry for comparison.

Three important points should be made. Most importantly, the wakefield shows prompt behavior at $t = t_0$, having a completely negligible precursor with a large contrast of at least 10^6,

lending strong credence to the accuracy of the phase calculation. Secondly, there are many orders of the wakefields, and the orders are much widely separated in time for the π scattering geometry than for σ. This is due to the fact that the bandwidth of the reflection in the π geometry is generally much narrower than that of σ. Finally, the amplitude of the σ geometry is much stronger than that of π, as it was the very reason that the seeding crystal will be rotated to accommodate the rotation of the polarization of the LCLS-II hard X-ray FEL beam.

2.1.2 Input field of a simulated SASE field with a perfect wavefront

In this section, we show the results for an input field from a single realization of a S2E simulation (Marcus, 2017), which exhibits the spiky nature of a SASE beam, not only in amplitude but also in phase across the pulse duration, which was about 50 fs. The intensity of the wakefield is shown in Figure 9, Figure 10, and Figure 11, for photon energies of 12, 8 and 4 keV, respectively.

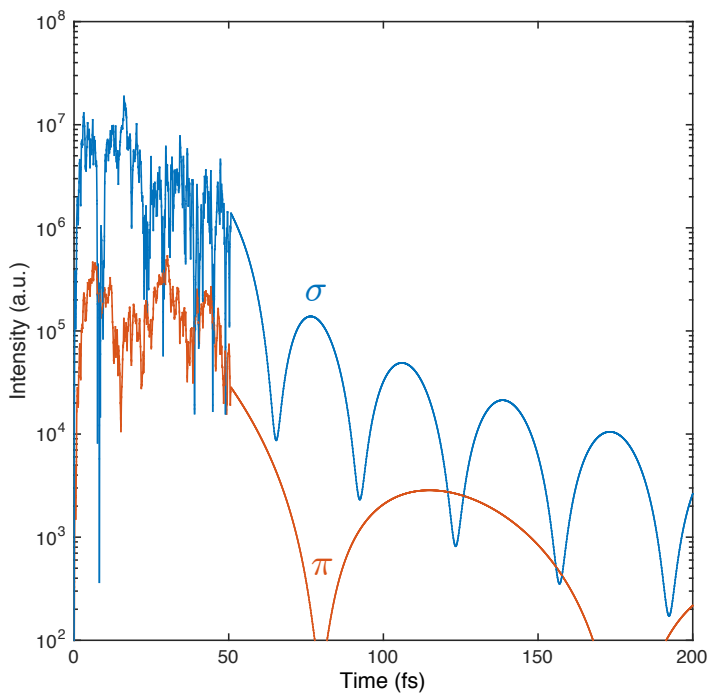

Figure 9. The wakefield intensity using a simulated SASE input field and including only the Forward Bragg Diffraction (FBD) part of the total transmitted beam at 12 keV of the diamond [004] symmetric reflection. The light blue curve is for the σ scattering geometry, and the brown curve for the π geometry for comparison.

The three important conclusions described in Section 2.1.1 for a Green's function input are still valid for a simulated SASE input, although the prompt behavior is now masked by the long pulse duration which starts at $t = 0$. An additional interesting but somewhat unexpected result is that the wakefield outside of the original input pulse exhibits the same smooth appearance as in Figure 6 or other figures for a Green's function input, very much devoid of the spikiness of the input field. In Figure 11 for photon energy at 4 keV, however, the amplitude of the wavefield also shows large variations in time, but on a time scale larger than that of the wakefield itself, mimicking the long time scale variation in intensity of the input SASE field, which is lacking in those for the 12 or 8 keV case in the particular realization of the S2E simulation. It is worthwhile and quite important to use different SASE realizations to confirm this observation.

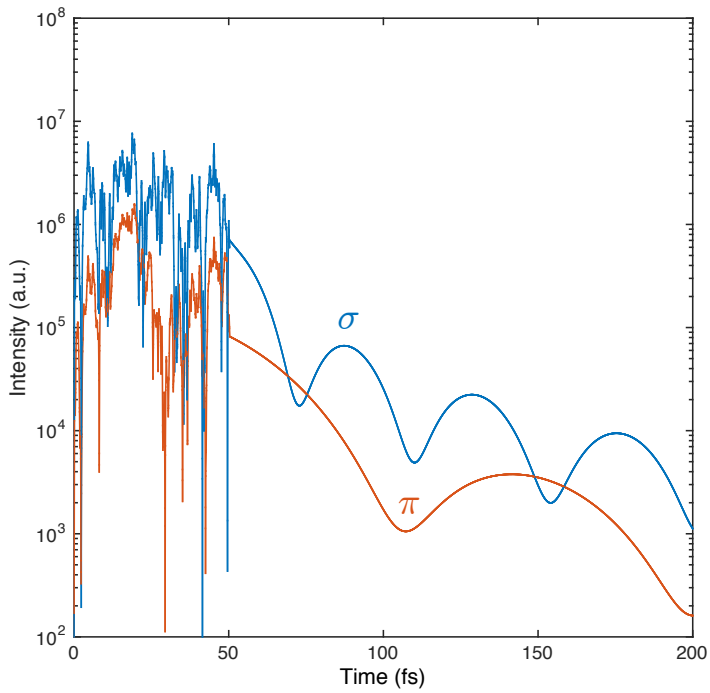

Figure 10. The wakefield intensity using a simulated SASE input field and including only the Forward Bragg Diffraction (FBD) part of the total transmitted beam at 8 keV of the diamond [004] symmetric reflection. The light blue curve is for the σ scattering geometry, and the brown curve for the π geometry for comparison.

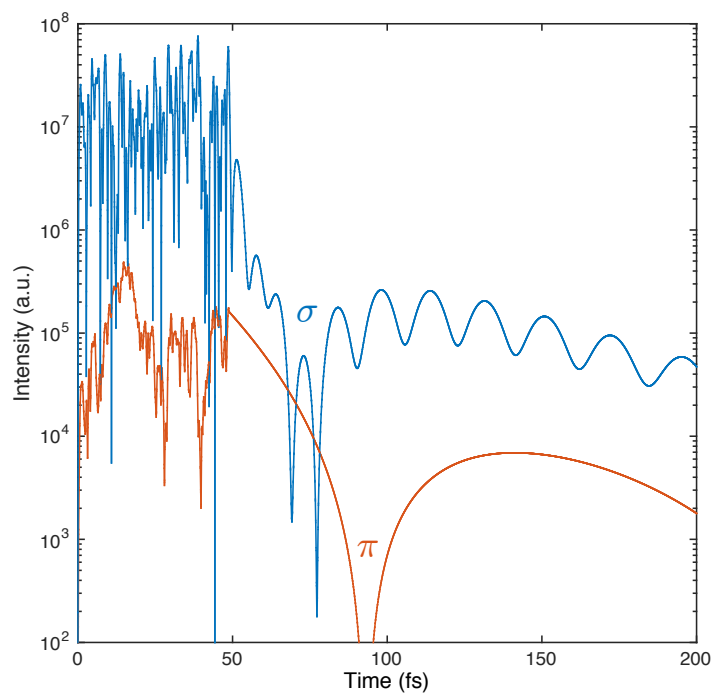

Figure 11. The wakefield intensity using a simulated SASE input field and including only the Forward Bragg Diffraction (FBD) part of the total transmitted beam at 4 keV of the diamond [111] asymmetric reflection off a [001] cut. The light blue curve is for the σ scattering geometry, and the brown curve for the π geometry for comparison.

2.2 Wakefields for strained crystals emulated by wavefront distortions

To calculate the impact of lattice imperfections on the wakefield, one could in principle make use of rigorous but difficult methods like the multi-lamellar approximation for bent crystals or the Penning-Polder approximation for bent Laue crystals, or solving the Takagi-Taupin equations for X-ray dynamical scattering from strained crystals (Takagi and Wills 1962; Taupin, 1964). Instead, we have taken a more practical and convenient approach by casting the problem in a different light, i.e., re-formulating the calculation of a strained crystal irradiated by a plane wave of a perfectly flat wavefront to that of a perfect crystal by a plane wave of a distorted wavefront. Additional assumption is also made that a flat wavefront can still be defined locally by the local curvature, and an average wavefront then defines the direction of beam propagation. No proof of the validity of this re-formulation will be given although similar treatment has been used previously, and the findings described below should be taken as an approximation to provide some quantitative assessment of a situation whose understanding could otherwise become rather intractable. Again, we first show the results on strained crystals using an input field of a) a Green's function at a small time offset, and b) simulated SASE field generated from S2E simulations (Marcus, 2107), for three different photon energies at 4, 8 and 12 keV.

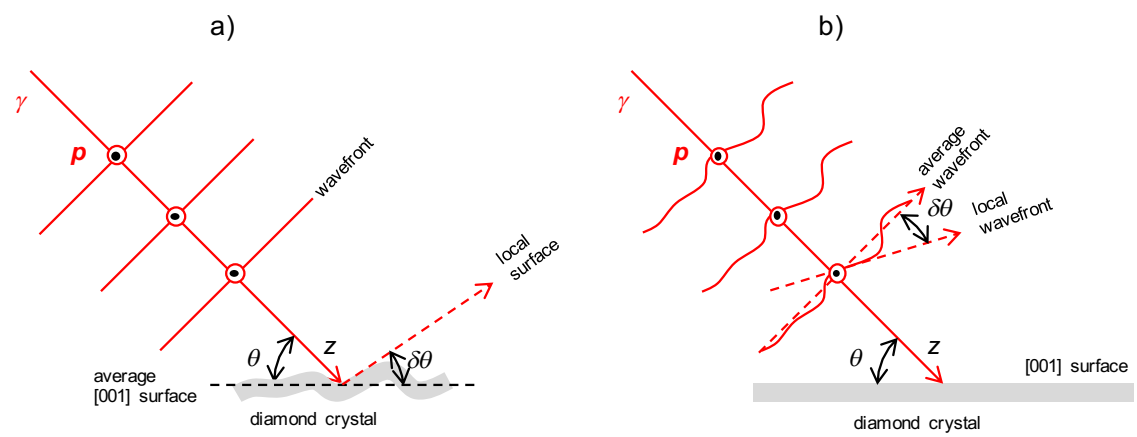

Figure 12. a) Incident FEL beam onto a distorted diamond crystal. The incident angle is given by the angle θ between the beam propagation direction z and the average surface (for symmetric reflections), with a correction term proportional to the angle $\delta\theta$ between the local surface and the average surface. b) Equivalent geometrical representation in terms of a perfect crystal but a distorted wavefront. For asymmetric reflections, the incidence angle must also be modified by the asymmetric angle Θ. $\boldsymbol{p}$ is a unit vectors, indicating the polarization in the σ scattering geometry.

A beam with a perfect wavefront is assumed to be incident onto a strained or distorted crystal in a symmetric reflection, the local incident angle θ_l is given by the angle θ between the beam propagation direction z and the average crystal surface with a correction term given by the angle $\delta\theta$ between the local and the average surfaces, as illustrated in Figure 12 a). This can be represented equivalently by a beam with a distorted wavefront incident onto a perfectly flat crystal, the local incident angle θ_l is given by the angle θ between the beam propagation direction z and the perfect crystal surface with a correction term given by the angle $\delta\theta$ between the local and the average wavefront, as illustrated in Figure 12 b). For asymmetric reflections, the incidence angle is also modified by the asymmetric angle Θ. Three reflections were used to cover the energy range, including the symmetric [004] at 12 keV, symmetric [004] at 8 keV, and asymmetric [111] at 4 keV using the [001] cut with an asymmetric angle Θ of 54.7356° from the

surface. The scattering is again in the σ geometry as shown in Figure 4. The thickness of the diamond is assumed to be 100 μm.

2.2.1 Input field of a Green's function in time with a distorted wavefront

First, we show the results for an input field of a quasi- delta-function in time at t_0 = 2.536 fs, which was assumed to have the a Gaussian lineshape with an arbitrary maximum and a FWHM of 0.082 fs (in intensity), and a flat phase across the pulse duration. The intensity of the wakefield and phase are shown in Figure 13 and Figure 15, for photon energy of 12 keV, and Figure 15 and Figure 16 for 8 keV, respectively. For each energy, the wakefield is calculated for different distortion angles at 1, 10, 100, and 1000 μdeg as the incidence angles, with 1 μdeg = 17.45 nrad. For comparison, the natural divergence of an X-ray FEL at 8 keV is about 2.5 μrad or 143 μdeg. The Darwin width of the diamond [004] reflection is about 17 μrad, or 974 μdeg.

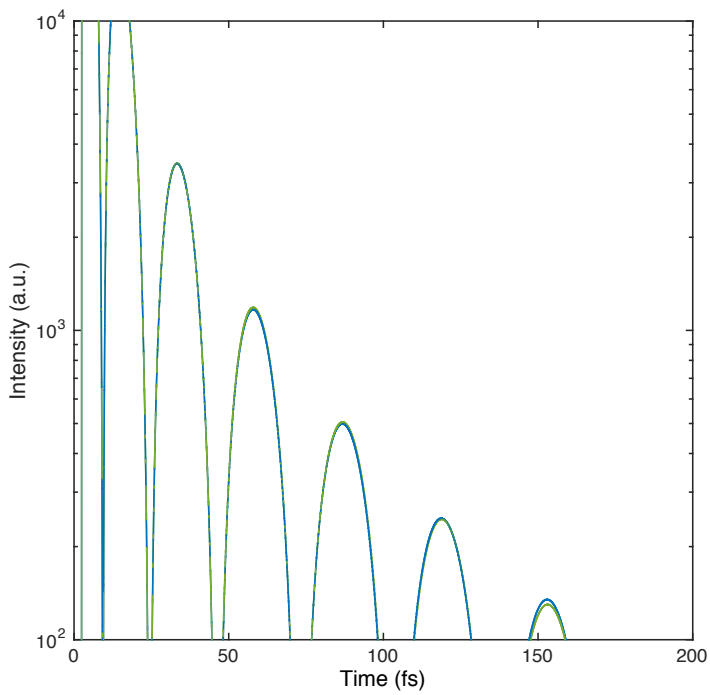

Figure 13. The wakefield intensity including only the Forward Bragg Diffraction (FBD) part of the total transmitted beam at 12 keV of the diamond [004] symmetric reflection in the σ scattering geometry. The light blue curve is at the Bragg angle θ_0 = 35.404513°, and the light green curve at negative 1 mdeg from θ_0 but is barely differentiable from that on Bragg. The intensities at 1, 10 and 100 μdeg were not shown for the sake of clarity.

The calculated wavefield intensities at 12 keV at different incidence angles shown in Figure 13 have barely any discernable differences even for distortion angles as large as 1 mdeg. In contrast, the phase shown in Figure 14 reveals appreciable change from that of exact on-Bragg incidence, and depends linearly on time within the regions of large phase jumps corresponding to the "troughs" of the wavefield amplitude. The rate of the linear phase change increases with the magnitude of the distortion angle $\delta\theta$ from the Bragg condition, and is positive for negative $\delta\theta$s, and vice versa. The similar behaviors can be observed in intensity and phase at 8 keV as shown in Figure 15 and Figure 16, although the rate of linear phase change is smaller than at 12 keV for the same deviation angle $\delta\theta$.

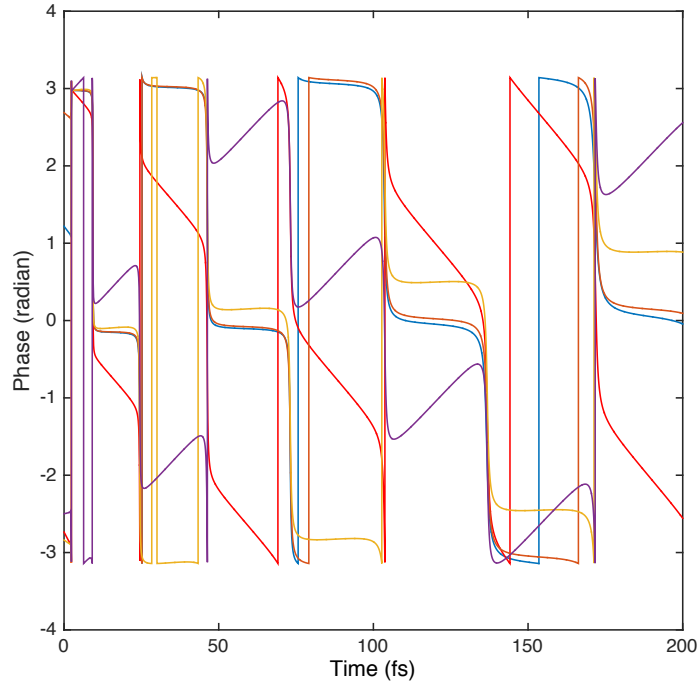

Figure 14. The wakefield phase (unwrapped) including only the Forward Bragg Diffraction (FBD) part of the total transmitted beam at 12 keV of the diamond [004] symmetric reflection in the σ scattering geometry. The light blue curve is at the Bragg angle θ_0 = 35.404513°, and the dark brown, light brown, and purple curves are at negative 1, 10, and 100 μdeg from θ_0, respectively. The red curve is for positive 100 μdeg from θ_0, which clearly shows symmetric dependence.

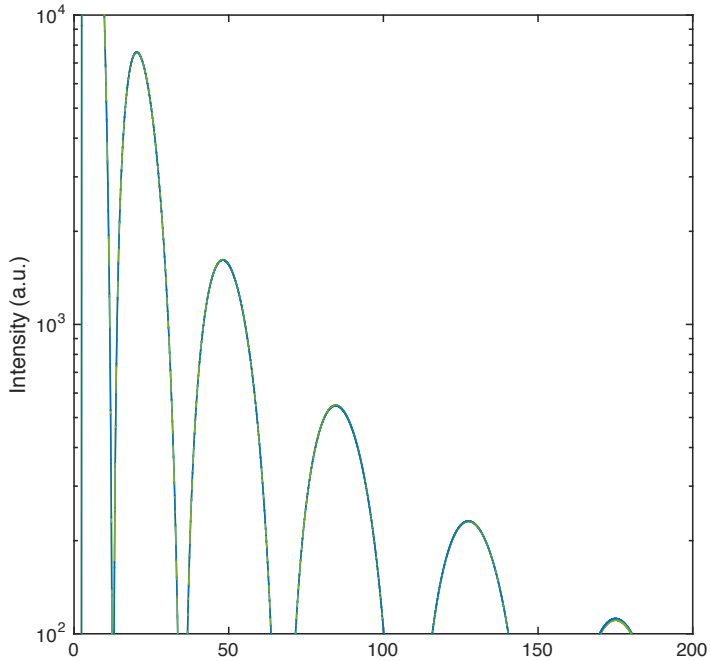

Figure 15. The wakefield intensity including only the Forward Bragg Diffraction (FBD) part of the total transmitted beam at 8 keV of the diamond [004] symmetric reflection in the σ scattering geometry. The light blue curve is at the Bragg angle θ_0 = 60.344732°, and the light green curve at negative 1 mdeg from θ_0 but is barely differentiable from that on Bragg.

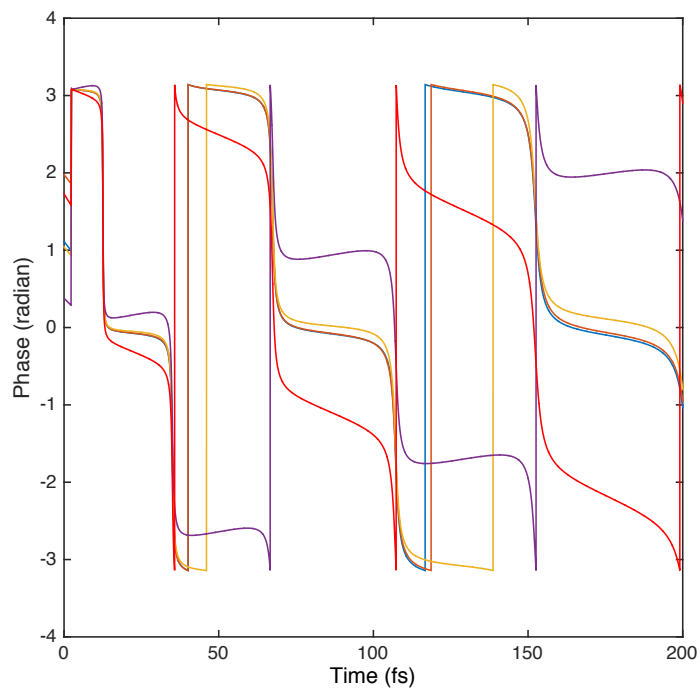

Figure 16. The wakefield phase (unwrapped) including only the Forward Bragg Diffraction (FBD) part of the total transmitted beam at 8 keV of the diamond [004] symmetric reflection in the σ scattering geometry. The light blue curve is at the Bragg angle θ_0 = 60.344732°, and the dark brown, light brown, and purple curves are at negative 1, 10, and 100 μdeg from θ_0, respectively. The red curve is for positive 100 μdeg from θ_0, which clearly shows symmetric dependence.

A linear phase change in time $r_\phi = d\phi/dt$ is equivalent to a shift or dispersion in frequency or energy of the seed field. According to the Bragg condition, $2d\sin\theta_0 = \lambda$, the change in energy is simply given by $r_\phi = \delta\varepsilon = -\,\varepsilon\bullet\mathrm{ctan}\theta_0\delta\theta$. For diamond [004], $r_\phi = -1.6883\times10^4\delta\theta$ eV at 12 keV and $r_\phi = -4.5549\times10^3\delta\theta$ eV at 8 keV, respectively. For example, at negative 100 μdeg, r_ϕ = 29.5 meV at 12 keV and r_ϕ = 7.9 meV at 8 keV, comparing to the Darwin width (equivalent to FWHM) of the reflection of 0.125 eV at 12 keV and 0.080 eV at 8 keV, respectively, or a 1×10^{-5} relative bandwidth. Therefore, the effect of a distorted crystal on the seed field is essentially having spatial variation of the seeding energy depicted below.

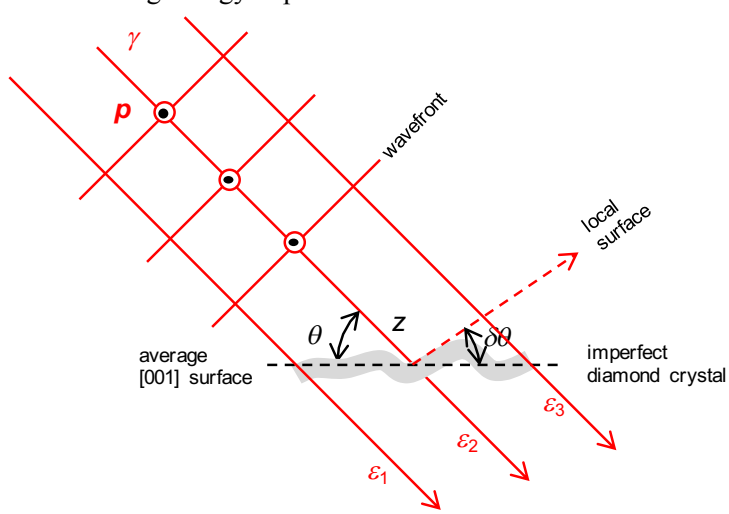

The tolerance on the level of imperfection in the crystal can be now defined. The flatness of the crystals within the footprint of the incident beam should be that the growth in the bandwidth of the seed due to crystal distortions or strains should be better than what is required by the seeding performance requirement itself. For example, at 8 keV, the optical period of the X-ray radiation is $T_0 = \lambda/c = 0.52$ attoseconds, where c is the speed of light. For a pulse of duration T, a transform-limited seed must have a bandwidth better than T_0/T, which is about $2.1\text{x}10^{-5}$ for $T = 25$ femtoseconds. The Diamond [004] reflection should meet this requirement by a factor of 2. Thus, as long as the crystal distortions are less than what is equivalent to 0.080 eV at 8 keV, or 1 mdeg ($r_\phi \sim 80$ meV) or 17 μrad, then the distortion will not impact the seeding performance. At 12 keV, the situation is little more demanding, a similar estimate gives the bandwidth limit at $1.4\text{x}10^{-5}$ for $T = 25$ femtoseconds, and the distortion limit at 400 μdeg ($r_\phi \sim 125$ meV) or 7.4 μrad. The natural divergence of the FEL beam is on the order of 2.5 μrad, so it would not have any real significant impact on the bandwidth of the seed field, as this was more or less supported experimentally (Amann, *et. al*, 2012).

2.2.2 Input field of a simulated SASE field with a distorted wavefront

In this section, we show the results for an input field from a single realization of a S2E simulation (Marcus, 2017), which exhibits the spiky nature of a SASE beam, not only in amplitude but also in phase across the pulse duration, which was about 50 fs. The intensity of the wakefield and phase are shown in Figure 17 and Figure 18 for photon energy of 12 keV, and Figure 19 and Figure 20, for 8 keV, respectively. For each energy, the wakefield is calculated for different distortion angles at 1, 10, 100, and 1000 μdeg as the incidence angles, with 1 μdeg = 17.45 nrad.

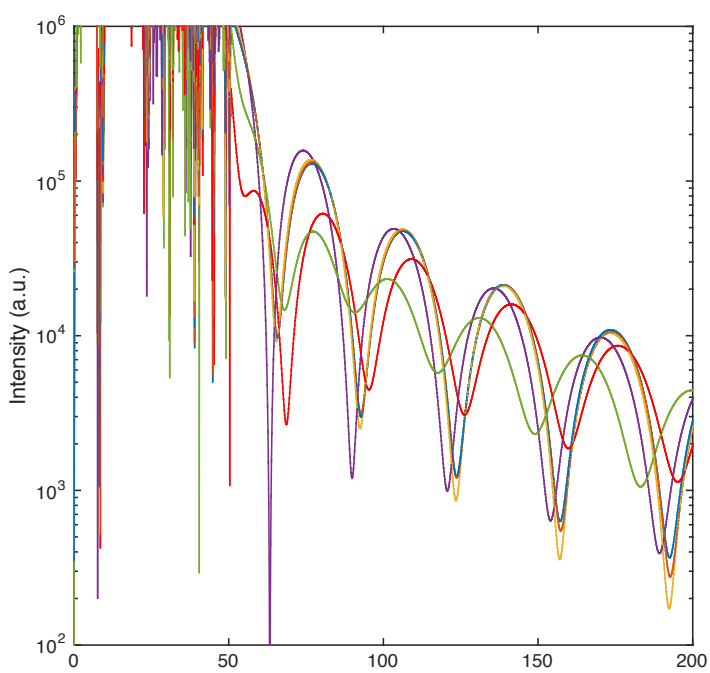

Figure 17. The wakefield intensity including only the Forward Bragg Diffraction (FBD) part of the total transmitted beam at 12 keV of the diamond [004] symmetric reflection in the σ scattering geometry. The light blue curve is at the Bragg angle $\theta_0 = 35.404513°$.

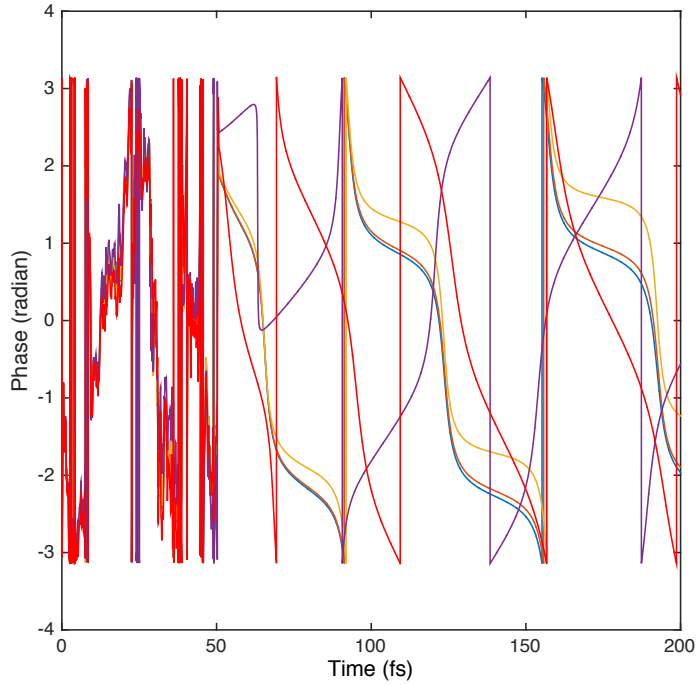

Figure 18. The wakefield phase (unwrapped) including only the Forward Bragg Diffraction (FBD) part of the total transmitted beam at 12 keV of the diamond [004] symmetric reflection in the σ scattering geometry. The light blue curve is at the Bragg angle θ_0 = 35.404513°, and the dark brown, light brown, and purple curves are at negative 1, 10, and 100 μdeg from θ_0, respectively. The red curve is for positive 100 μdeg from θ_0, which clearly shows symmetric dependence.

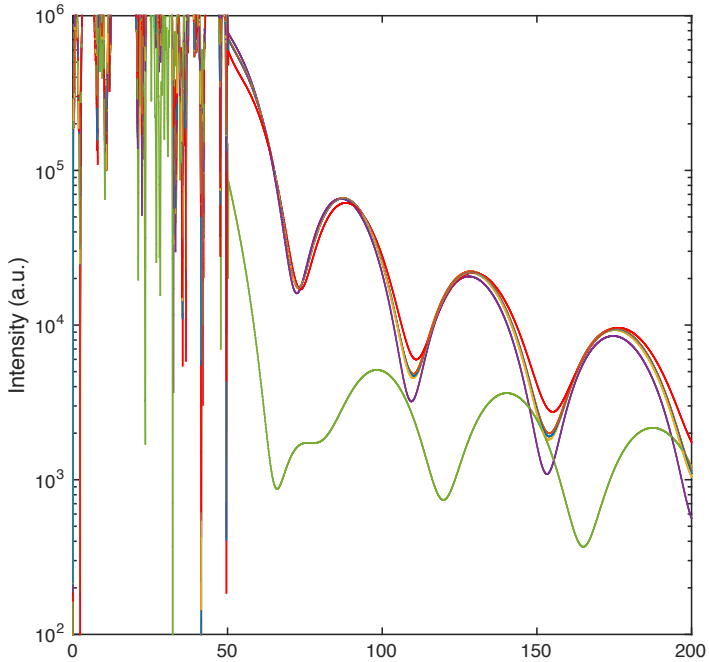

Figure 19. The wakefield intensity including only the Forward Bragg Diffraction (FBD) part of the total transmitted beam at 8 keV of the diamond [004] symmetric reflection in the σ scattering geometry. The light blue curve is at the Bragg angle θ_0 = 60.344732°.

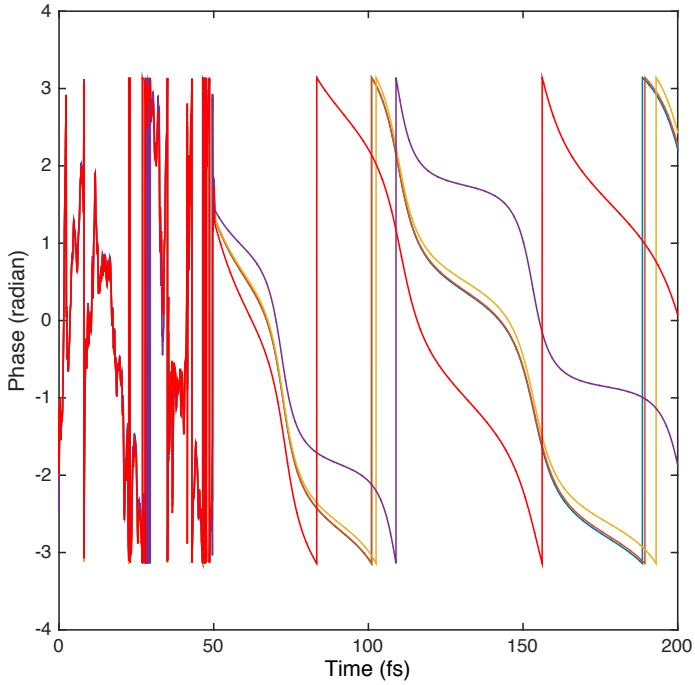

Figure 20. The wakefield phase (unwrapped) including only the Forward Bragg Diffraction (FBD) part of the total transmitted beam at 8 keV of the diamond [004] symmetric reflection in the σ scattering geometry. The light blue curve is at the Bragg angle θ_0 = 60.344732°, and the dark brown, light brown, and purple curves are at negative 1, 10, and 100 μdeg from θ_0, respectively. The red curve is for positive 100 μdeg from θ_0, which clearly shows symmetric dependence.

3 References

Amann, J., Berg, W., Blank, V., Decker, F.-J., Ding, Y., Emma, P., Feng, Y., Frisch, J., Fritz, D., Hastings, J. *et al*. (2012). *Nature Photon*. **6**, 693.

Geloni, G., Kocharyan, V., and Saldin, E. (2010). *arXiv:1008.3036v1*.

Geloni, G., Kocharyan, V., and Saldin, E. (2011). *J. Mod. Opt*. **58**, 1391.

Lindberg, R. R., and Shvyd'ko, Y.V. (2012). *Phys. Rev. ST Accel. Beams* **15**, 050706.

Marcus, G. (2017). unpublished.

Shvyd'ko, Y.V., and Lindberg, R. R. (2012). *Phys. Rev. ST Accel. Beams* **15**, 100702.

Takagi, S. and Wills, H.H. (1962). *Acta. Cryst*. **15**, 1311.

Taupin, D. (1964). *Bull. Soc. Fr. Mineral. Crystallogr*. **87**, 469.